CFD Investigation of 3D Vertical Axis Wind Turbine Models: Insights from Blade Tip Effects

Taurista Perdana Syawitri[1,*], Yufeng Yao[2], Jun Yao[2], Budi Chandra[2], Amiral Aziz[1], Didik Rostyono[1], Rudi Purwo Wijayanto[1], Arfie Ikhsan Firmansyah[3], Agustina Putri Mayasari[4], Ario Witjakso[1]

[1]Research Center for Energy Conversion Technology, National Research and Innovation Agency, Republic of Indonesia
[2]School of Engineering, University of the West of England, Bristol, United Kingdom
[3]Directorate of Policy Formulation for Research, Technology, and Innovation, National Research and Innovation Agency, Republic of Indonesia
[4]National Research and Innovation Agency, Republic of Indonesia

*Author to whom correspondence should be addressed:
E-mail: taur003@brin.go.id

(Received June 04, 2025; Revised September 29, 2025; Accepted December 15, 2025)

Abstract: This study presents a detailed three-dimensional (3D) numerical analysis of Vertical Axis Wind Turbines (VAWTs) to investigate aerodynamic performance and 3D flow effects. Building upon a validated two-dimensional (2D) model, the 3D computational domain leverages symmetry boundary conditions to reduce computational costs, modelling only half of the rotor blades. The 3D domain's dimensions and grid resolutions are in alignment with previous 2D studies, with modifications for span-wise and blade tip regions. A hybrid turbulence model, SBES with Transition SST, is employed, yielding moment coefficient predictions within an acceptable discrepancy range compared to experimental data. Grid independence is established via systematic grid refinement in span-wise and far-field sub-domains, ensuring accurate representation of 3D flow characteristics. Results highlight significant deviations in aerodynamic performance along span-wise positions, particularly at azimuthal ranges of 45°-150° and 210°-270° respectively, attributed to dynamic stall, vortex interactions, and blade tip effects. While the 3D CFD model underpredicts power coefficients compared to experimental data, it captures three-dimensional flow phenomena absent in 2D simulations. Contour plots of span-wise vorticity reveal consistent blade tip vortex formation and dissipation across azimuthal positions, underscoring the reduced aerodynamic impact beyond the tip. The study confirms the need for refined turbulence models and additional experimental validation to enhance 3D VAWT performance prediction.

Keywords: blade tip effect; blade tip vortex; computational fluid dynamics; dynamic stall; three-dimensional flows; vertical axis wind turbines

1. Introduction

Computational Fluid Dynamics (CFD) has become the predominant analytical tool in recent investigations of Vertical Axis Wind Turbines (VAWTs), owing to the inherently complex aerodynamic phenomena that are challenging to characterize through experimental approaches alone [1)]. VAWTs are subject to dynamic stall, vortex shedding, wake interactions, and blade tip effects, all of which exert a significant influence on their aerodynamic performance and efficiency [2,3)]. Experimental characterisation of these phenomena is further constrained by the limitations of wind tunnel and field testing, including high costs and difficulties in resolving intricate flow structures [4)]. By contrast, CFD enables comprehensive exploration of blade and wake flow dynamics under controlled conditions, while also facilitating systematic assessment of design variables such as blade geometry [5)], aspect ratio [6)], and operating conditions [7)], thereby supporting the optimisation of VAWT performance [8)].

CFD studies of VAWTs are commonly performed using either two-dimensional (2D) or three-dimensional (3D) approaches. In recent years, 2D CFD has gained popularity

Cite: T. Syawitri et al., "CFD Investigation of 3D Vertical Axis Wind Turbine Models: Insights from Blade Tip Effects". Evergreen, 12 (04) 2146-2164 (2025). https://doi.org/10.5109/7402644.

as a computationally efficient method for analysing VAWT performance, offering valuable insights into wake development, flow separation, and dynamic stall [9,11] while enabling rapid design iterations [12]. Such models, typically based on mid-plane cross sections, are particularly useful in early-stage optimisation of blade profiles [13], chord-to-radius ratios [14], and tip-speed ratio (*TSR*s) [15]. However, the simplification inherent in 2D modelling neglects key three-dimensional effects, such as tip vortices, span-wise flow, and turbine end effects, that strongly influence real-world performance [16]. Studies have shown that 3D simulations often predict lower power coefficients (C_p) than 2D models, especially at high *TSR*s where wake interactions dominate [17,18]. Moreover, the assumption of infinite blade height and the limited representation of dynamic stall recovery [19,20] can lead to overestimations of aerodynamic forces and reduced accuracy under turbulent or gusty conditions [21,22].

Recent advancements in CFD have enabled detailed investigations of 3D VAWT models, providing deeper insight into aerodynamic behaviour. Unlike two-dimensional approaches, 3D simulations capture span-wise cross flow and unsteady aerodynamics [23,26], allowing more accurate performance prediction under realistic conditions [27]. They also facilitate systematic analysis of design parameters such as rotor spacing [28], pitch control [29], and blade geometry [30]. To address the unsteady flow structures characteristic of VAWTs, high-fidelity turbulence models including Large Eddy Simulation (LES) [31,32] and hybrid Reynolds-Averaged Navier–Stokes (RANS)-LES [33], together with adaptive mesh refinement [34,35], have been increasingly adopted. Key findings highlight the significant role of tip vortices, which contribute to energy losses [36,38], but can be mitigated through advanced blade designs such as winglets [39]. Wake dynamics also emerge as critical, particularly in wind farm arrays where staggered or counter-rotating configurations may enhance energy capture through constructive interference [40]. Nevertheless, the high computational demands of 3D CFD limit its application in parametric or optimisation studies, while persistent discrepancies with experimental data underscore the need for improved turbulence models and boundary conditions tailored to VAWTs.

This study investigates blade tip effects on VAWT performance through a 3D CFD analysis of a three-straight-bladed model, extending a previously validated 2D approach [41,42]. To reduce computational cost, only the upper half of the rotor was modelled using symmetry boundary conditions [43], with the domain divided into control, rotating, and far-field regions and meshed via CutCell techniques. A turbulence model sensitivity analysis identified the Stress-Blended Eddy Simulation (SBES) with Transition Shear Stress Transport (TSST) as the most reliable for predicting power coefficients. Simulations were performed at medium *TSR*s, where VAWTs typically achieve optimal efficiency. The objectives are (1) to compare 3D performance with experimental and 2D results and (2) to examine span-wise variations in aerodynamic behaviour and flow structures. The results reveal the influence of 3D flow effects, particularly tip vortex formation and regions of aerodynamic inefficiency, providing a foundation for future VAWT design optimisation and sustainable energy applications.

2. Model description

In this 3D simulation study, experimental data from Castelli, Englaro, and Benini [44] and validated 2D results [41,42] were compared with the present simulations. To improve efficiency, symmetry boundary conditions were applied at the rotor mid-span, allowing only the upper portion of the VAWT to be modelled, as recommended by Howell et al. [43]. The VAWT model is presented in Figure 1a, while the computational domain and boundary specifications, including inlet, outlet, and symmetry planes, are shown in Figure 1b. The domain dimensions replicate those of the earlier 2D study [41,42], with a height equivalent to approximately 11 times the rotor height (or roughly 31 rotor radius) following Elsakka [45], ensuring accurate representation of the flow field.

The boundary conditions and meshing parameters for the 3D model align with those previously validated in the 2D domain [41,42]. The 3D domain is divided into three primary regions, mirroring the 2D configuration (see Figure 2a): a surrounding far-field zone, a rotating region around the turbine, and a control zone encompassing each blade. A non-conformal "fluid-to-fluid" interface connects the rotating and far-field domains. Internal surfaces define the boundaries between the control and rotating zones to ensure smooth fluid flow. As shown in Figure 2b, the height of the rotating sub-domain extends by one chord length (0.0858 m) above the blade tip, accommodating tip vortex development. Prior studies with similar Reynolds numbers suggest that vortices extend approximately 0.04 m beyond the blade tip for a chord of 0.06 m [46], validating this extension.

In this study, ANSYS Fluent v19 was employed for the CFD simulations, as it offers extensive physical modelling capabilities encompassing fluid flow, turbulence, heat transfer, and chemical reactions, together with a broad selection of turbulence models and a comparatively straightforward implementation framework. For turbulence modelling, the SBES approach coupled with the TSST model was adopted, based on its reliable performance in the 2D analysis [41,42], particularly in accurately predicting C_p.

The SBES formulation combines the RANS and LES methodologies through a blending function (see Eqs. 1 and

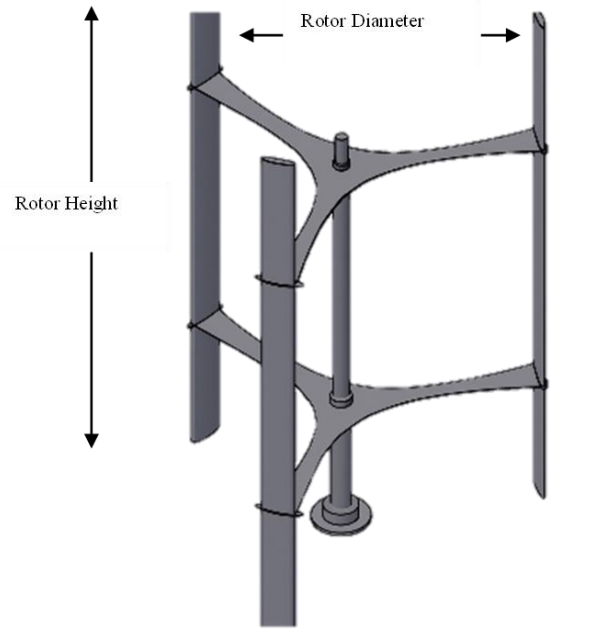

(a) VAWT model [41)]

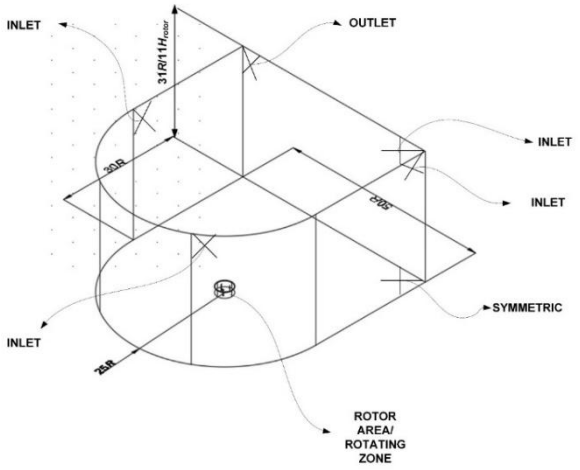

(b) Primary boundary conditions and dimensions of the three-dimensional computing domain (the illustration is not to scale)

Fig. 1: 3D computational model

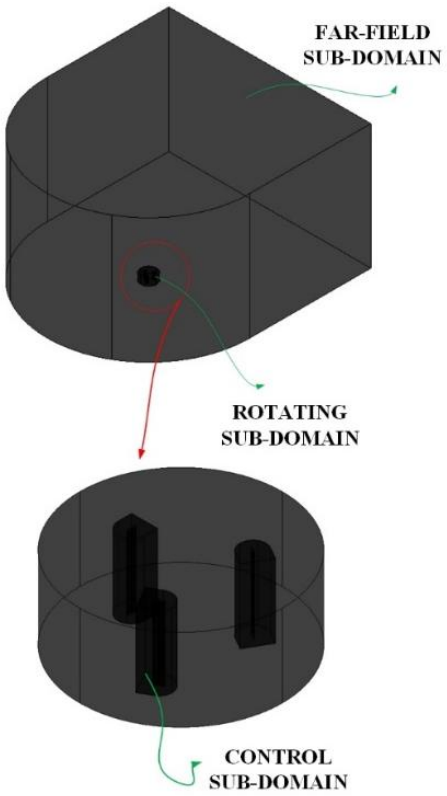

(a) Subdomain detail in the 3D model (the drawing is not to scale)

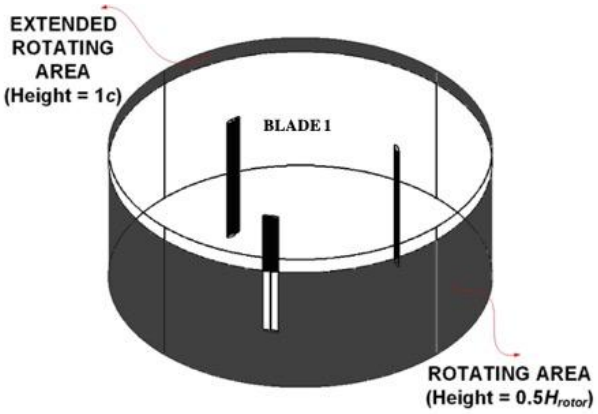

(b) Rotating sub-domain with height extension

Fig. 2: Detail of the 3D computational domain and its sub-domains (the drawing is not scaled)

2):

$$\tau_{i,j,k}^{SBES} = f_{SBES}\tau_{i,j,k}^{RANS} + (1 - f_{SBES})\tau_{i,j,k}^{LES} \quad (1)$$

$$\upsilon_t^{SBES} = f_{SBES}\upsilon_t^{RANS} + (1 - f_{SBES})\upsilon_t^{LES} \quad (2)$$

where $\tau_{i,j,k}$ and υ_t are turbulence stress tensor and turbulent kinematic viscosity, respectively. $\tau_{i,j,k}^{RANS}$ and υ_t^{RANS} are the contribution from the TSST model. $\tau_{i,j,k}^{LES}$ and υ_t^{LES} are the sub-grid scale turbulence stress tensor and turbulent kinematic viscosity, respectively, used in LES. f_{SBES} is a blending function ensuring a smooth transition between the RANS and LES regions. RANS is applied in the near-wall region, while LES is activated in the separated flow and wake regions, enabling improved resolution of unsteady vortex structures.

To capture laminar-to-turbulent transition effects, the Transition SST model introduces two additional transport equations (see Eqs. 3 and 4) for intermittency (γ) and the transition onset momentum-thickness Reynolds number ($Re_{\theta t}$):

$$\frac{\partial(\rho\gamma)}{\partial t} + \frac{\partial(\rho U_j\gamma)}{\partial x_j} = P_\gamma - E_\gamma + \frac{\partial}{\partial x_j}\left[(\mu + \sigma_f\mu_t)\frac{\partial\gamma}{\partial x_j}\right] \quad (3)$$

$$\frac{\partial(\rho Re_{\theta t})}{\partial t} + \frac{\partial(\rho U_j Re_{\theta t})}{\partial x_j} = P_{\theta t} + \frac{\partial}{\partial x_j}\left[(\mu + \sigma_\theta\mu_t)\frac{\partial Re_{\theta t}}{\partial x_j}\right] \quad (4)$$

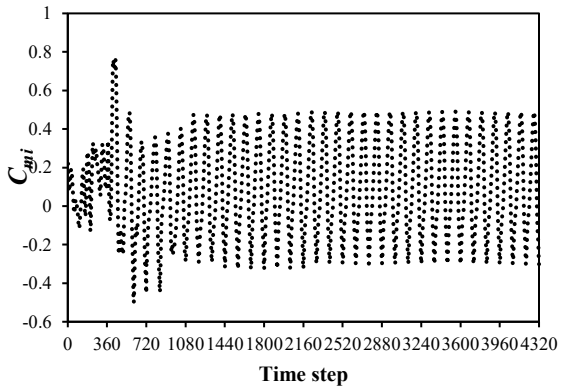

Fig. 3: Instantaneous moment coefficient (C_{mi}) over the first 12 revolutions/cycles

where ρ is the fluid density (kg/m^3), U is the fluid velocity (m/s), μ is the dynamic viscocity (Pa.s), μ_t is the turbulence dynamic viscosity (Pa.s), σ_f is the diffusion coefficient for the intermittency equation, and σ_θ is the diffusion coefficient for the transition-onset momentum-thickness Reynolds number. P_γ and E_γ represent the production and destruction of intermittency, respectively, while $P_{\theta t}$ is the source term for transition onset. These additional equations regulate turbulence production in separated shear layers, allowing accurate prediction of separation-induced transition. By coupling SBES with the Transition SST model, this framework balances computational cost and accuracy, enabling precise resolution of critical unsteady flow features such as dynamic stall, vortex shedding, tip vortex formation, and span-wise flow variations, which strongly influence VAWT aerodynamic performance.

Given the high computational load, the 3D simulation was performed only at the optimal TSR of 2.64, corresponding to the baseline turbine configuration. In line with Castelli et al. [44], time-averaged moment coefficient (Cm-ave) data were collected only after convergence, defined as a fluctuation of less than 1% over a single turbine revolution. This condition was met after 10 full rotations, as shown in Figure 3, with data acquisition beginning from the 11th cycle onward.

3. Grid discretisation

The mesh design for the 3D model reused the grid topology validated in the 2D study for both the rotating and control regions, featuring 174 elements around each blade cross-section. To ensure accurate boundary-layer resolution, the non-dimensional wall distance (y^+) value was maintained at approximately 1 around the blade surface. Span-wise, 40 elements were used to resolve half the blade height, with the height extension of the rotating zone subdivided into 10 elements. Mesh refinement near the blade tip is illustrated in Figure 4.

To manage computational demand, a different meshing strategy was applied in the far-field region of the 3D model compared to the 2D version. Larger elements were used where feasible, while fine meshing was maintained near the rotor and wake regions to preserve result accuracy. The far-field was meshed using the CutCell method [47], which constructs predominantly hexahedral grids arranged in a Cartesian layout. This technique provides a balanced grid growth rate and avoids excessive element skewness, thereby improving computational performance.

As depicted in Figure 5, the CutCell strategy enabled a more efficient and adaptable grid distribution compared to structured meshes, significantly reducing the total number of elements in the far-field region. Structured meshes are advantageous for capturing fine details near blade surfaces; however, the hybrid approach employed in this study achieves a balance between computational efficiency and detail accuracy.

4. Grid independence analysis

To ensure spatial resolution was adequate in all directions, the grid independence of the streamwise and transverse directions (x and y) relied on configurations already verified in earlier 2D work [41,42]. For the span-wise direction (z), additional tests were conducted with 35, 40, and 45 elements along the blade height, maintaining 10 elements in the extended rotor zone. Figure 6a shows that the distribution of instantaneous moment coefficients (Cmi) was largely unaffected by this variation. The difference in Cm-ave between the 35- and 40-element setups was 7.28%, while the variation between 40 and 45 elements dropped to 1.48%. Accordingly, 40 elements were applied along the blade span and 10 elements within the extended rotor zone, yielding a total of 50 span-wise elements for the subsequent simulations.

To validate grid independence in the far-field region, three

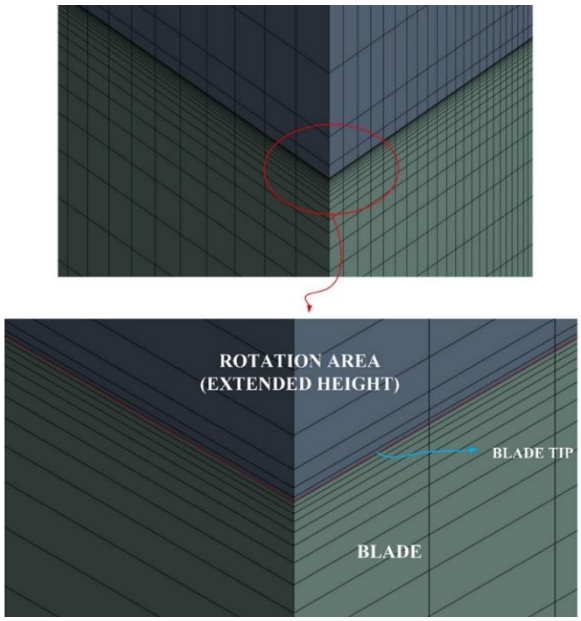

Fig. 4: Clustered grid around the tip of the blade

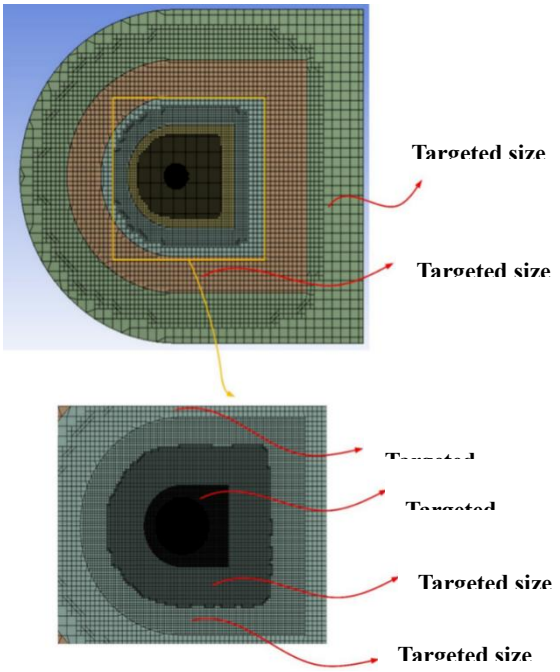

Fig. 5: Implement CutCell mesh in the far-field sub-domain

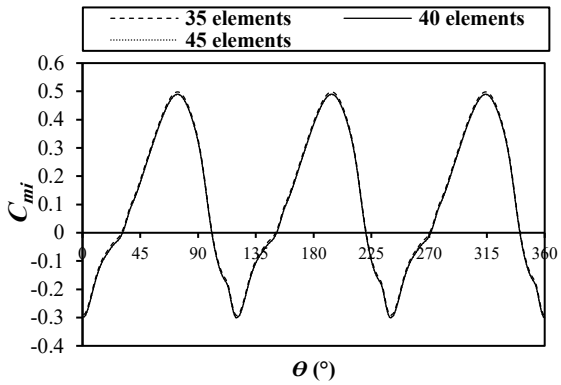

(a)

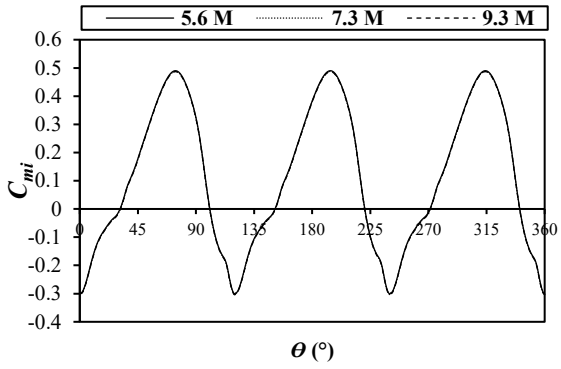

(b)

Fig. 6: C_{mi} comparison of the 3D model with (a) different number of elements along the span-wise direction and (b) various grids

mesh densities were assessed. The baseline grid consisted of 5,598,471 elements, while two denser versions were generated by increasing element counts by approximately

Table 1: The number of elements for each grid and its averaged moment coefficient prediction

Grid	Grid density ratio (relative to the baseline)	C_{m-ave}	% difference in C_{m-ave}
Baseline 5.6 M	1	0.11124	–
Refined 7.3 M	~1.3	0.10876	2.23
Most refined 9.3 M	~1.66	0.10700	2.91

30% and 66%, respectively (see Table 1). The number of elements in the blade cross-section (174), blade span-wise direction (40), and height extension (10) remained constant to isolate the effects of far-field mesh refinement. Figure 6b presents the results of this sensitivity test using the SBES with the Transition SST model. The simulations showed limited sensitivity to grid refinement, with the most refined mesh differing from the baseline by only 2.91% in Cm-ave values (see Table 1). Thus, the baseline configuration was deemed sufficient for the remainder of the study.

5. 3D simulation results

5.1. Validation of averaged power coefficient ($C_{p\text{-}ave}$)

Table 2 compares Cp-ave from experimental studies [44,48], 2D CFD simulations [41,42,44,49], and the present 3D CFD results evaluated at several span-wise positions along the rotor blade (see Figure 7). To quantify the deviation, the difference was evaluated using Eq. 5.

$$\%difference = \frac{\Delta C_{p-ave}}{C_{p-ave,experiment}} \, x \, 100\% \qquad (5)$$

where ΔC_{p-ave} denotes the difference between the $C_{p\text{-}ave}$ values obtained from experimental and simulation data.

At the rotor's mid-span, the 3D simulation tends to underestimate the $C_{p\text{-}ave}$ relative to experimental findings, while the 2D model slightly overestimates it. Notably, the 2D predictions closely follow prior findings [44,49]. This discrepancy arises because the 3D model captures complex three-dimensional flow effects, which the 2D approach cannot. The deviation of 0.47% in the 2D SBES-TSST model suggests high accuracy for planar flows.

At mid-span, the 3D SBES-TSST model underestimates $C_{p\text{-}ave}$ by approximately 7.48% when benchmarked against experimental data. This discrepancy grows toward the blade tip, peaking at 17.52%. A similar trend was noted in Elsakka's research [46], where deviations increased with radial distance due to a lower aspect ratio turbine that amplified tip loss effects (see Table 3). Across all span-wise positions, the average underestimation by the 3D model is about 13.13%.

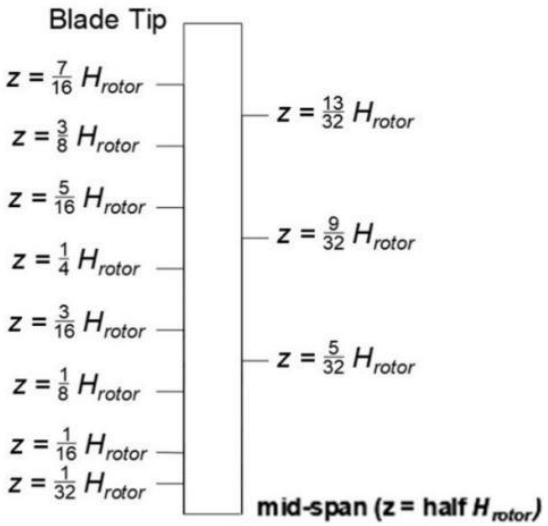

Fig. 7: Illustration depicting the significant span-wise locations within the rotating sub-domain, where H_{rotor} denotes the turbine's height

may stem from the hybrid turbulence model's limitations. While accurate in 2D cases [50], hybrid RANS-LES approaches, such as SBES, may exaggerate pressure loss and flow separation in complex turbulent regimes, leading to diminished moment coefficients in 3D. This suggests a need for improved turbulence modelling in three-dimensional simulations.

To improve accuracy, simulations using the standard SST turbulence model were conducted. While the 2D SST model shows a 13.78% discrepancy at a *TSR* of 2.64, its 3D application significantly reduces the deviation to only 1.17%, demonstrating its potential for enhanced accuracy. Nonetheless, SST still faces challenges in capturing phenomena like dynamic stall, trailing-edge vortex roll-up, and secondary vortex generation, indicating the need for more experimental validation. Despite the SBES-TSST model's 13.13% average deviation, its performance falls within the 9–16% range reported in similar 3D VAWT studies using hybrid turbulence models [33,50,51]. The experimental C_p values reported by Castelli et al. [48], based on averaged torque data, support the reliability of the comparison.

Table 2: Comparison between experimental power coefficient data [44,48] and the predicted average power coefficients from 2D and 3D models

Case	Turbulence Model	Span-wise location	$C_{p\text{-ave}}$	%difference from experiment	%difference from mid-span
Experimental data [44,48]	–	–	0.31741	–	–
Castelli, Englaro and Benini [44] (2D CFD)	RKE	Mid-span	0.56937	79.37765	–
Wang *et al*. [49] (2D CFD)	RKE	Mid-span	0.30364	4.34027	–
	SST	Mid-span	0.37407	17.85093	–
Present study (2D CFD)	RKE	Mid-span	0.37133	16.98658	–
	SST	Mid-span	0.36114	13.77542	–
	SBES with TSST	Mid-span	0.31892	0.47425	–
Present study (3D CFD)	SBES with TSST	Mid-span	0.29368	7.47721	–
		z = 1/32 H_{rotor}	0.29039	8.51446	1.12107
		z = 1/16 H_{rotor}	0.28737	9.46516	2.14861
		z = 1/8 H_{rotor}	0.28203	11.14694	3.96630
		z = 5/32 H_{rotor}	0.27966	11.89430	4.77406
		z = 3/16 H_{rotor}	0.27746	12.58823	5.52406
		z = 1/4 H_{rotor}	0.27349	13.83716	6.87393
		z = 9/32 H_{rotor}	0.27170	14.40114	7.48349
		z = 5/16 H_{rotor}	0.27002	14.92985	8.05492
		z = 3/8 H_{rotor}	0.26696	15.89387	9.09685
		z = 13/32 H_{rotor}	0.26557	16.33453	9.57312
		z = 7/16 H_{rotor}	0.26424	16.75070	10.02292
		Blade tip	0.26181	17.51727	10.85144
		Averaged 3D	0.27572	13.13468	6.11467

Table 3: Comparison of the predicted average moment coefficients between Elsakka [45] and the present study at various span-wise locations along the blade

Case	r (m)	H_{rotor} (m)	Aspect Ratio	Turbulence Model	Span-wise location	$C_{m\text{-}ave}$	% Difference from Mid-span
Elsakka [45]	0.850	1.2000	1.41176	SST	Mid-span	0.09400	–
					z = 3/8 H_{rotor}	0.07300	22.34043
					z = 13/32 H_{rotor}	0.06600	29.78723
				TSST	Mid-span	0.09100	–
					z = 3/8 H_{rotor}	0.05600	38.46154
					z = 13/32 H_{rotor}	0.05100	43.95604
Present study	0.515	1.4564	2.82796	SBES with TSST	Mid-span	0.11124	–
					z = 3/8 H_{rotor}	0.10112	9.09685
					z = 13/32 H_{rotor}	0.10059	9.57312

5.2. Span-wise blade aerodynamics

Figure 8 illustrates the C_{mi} of blade 1 over a full rotation at various span-wise positions. Significant variation is observed within the azimuthal ranges θ = 45°–150° and θ = 210°–270°, with minimal deviation elsewhere. These fluctuations are attributed to unsteady aerodynamic behaviour: during θ = 45°–150°, the blade experiences varying angles of attack, resulting in flow separation and potential dynamic stall [52]. Conversely, from θ = 210°–270°, the blade encounters vortices shed from upstream blades [52], amplifying aerodynamic loads, particularly near the blade tip. Figure 9 displays z-vorticity contours across several key azimuthal angles during the blade's rotation. Outside the highlighted azimuthal ranges, vortex shedding is weak and uniform along the span-wise direction, as shown in Figure 10b. Near the blade tip, vortex formation is minimal and dissipates rapidly within approximately 0.005 H_{rotor} from the tip. These results suggest limited influence of tip vortices outside the critical azimuthal zones.

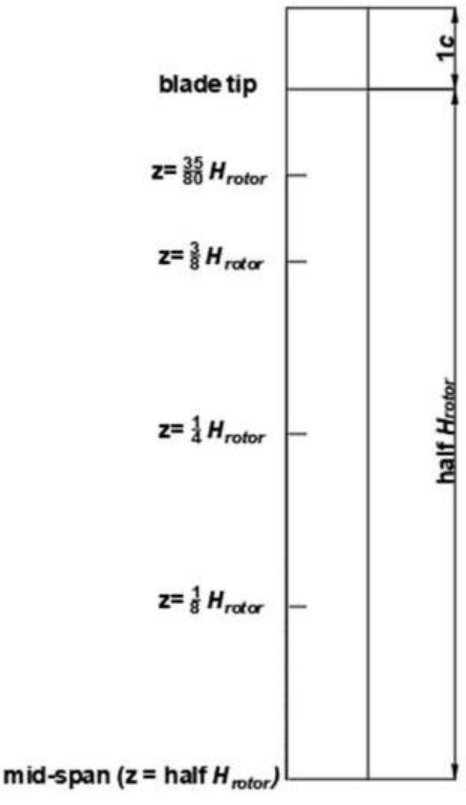

(a)

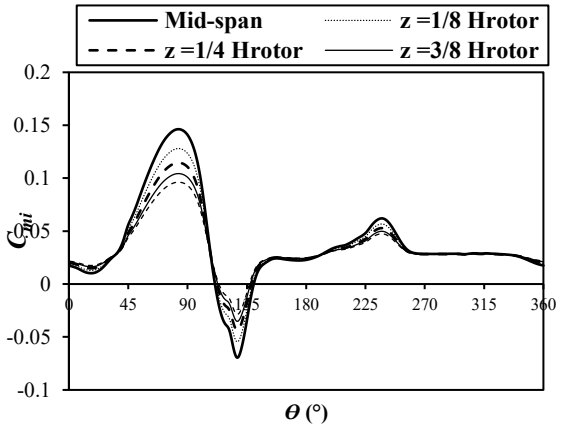

(b)

Fig. 8: (a) Diagram illustrating significant span-wise locations inside the rotating sub-domain and (b) C_{mi} of blade 1 at various locations along the span-wise direction of the blade

During the θ = 45°–150° range, enhanced trailing-edge vortex-shedding and dynamic stall are evident, especially in Figure 9b and Figure 9c. At θ = 135°, the blade develops pronounced trailing-edge roll-up vortices that merge with tip vortices beyond the mid-span. For instance, a detached vortex at z = 91/200 H_{rotor} travels outward and merges with a developing tip vortex at z = 47/100 H_{rotor} eventually stabilising around z = 19/40 H_{rotor}. This vortex structure at θ = 135° is notably stronger than that at θ = 30°.

Cite: T. Syawitri et al., "CFD Investigation of 3D Vertical Axis Wind Turbine Models: Insights from Blade Tip Effects". Evergreen, 12 (04) 2146-2164 (2025). https://doi.org/10.5109/7402644.

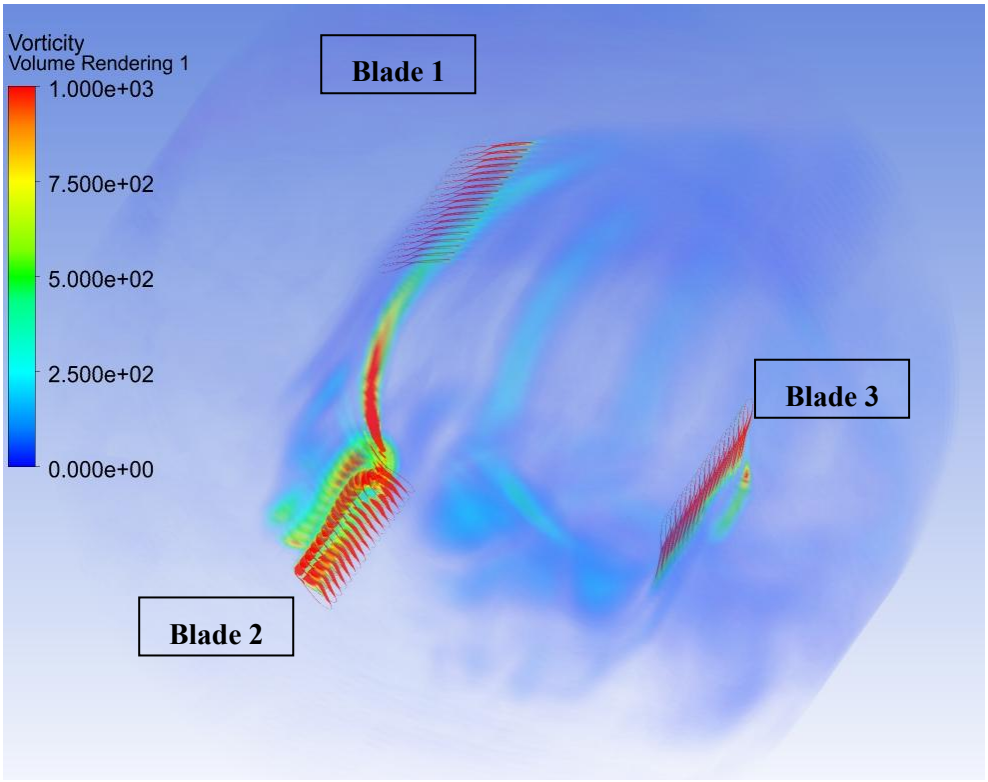

(a) θ = 30°

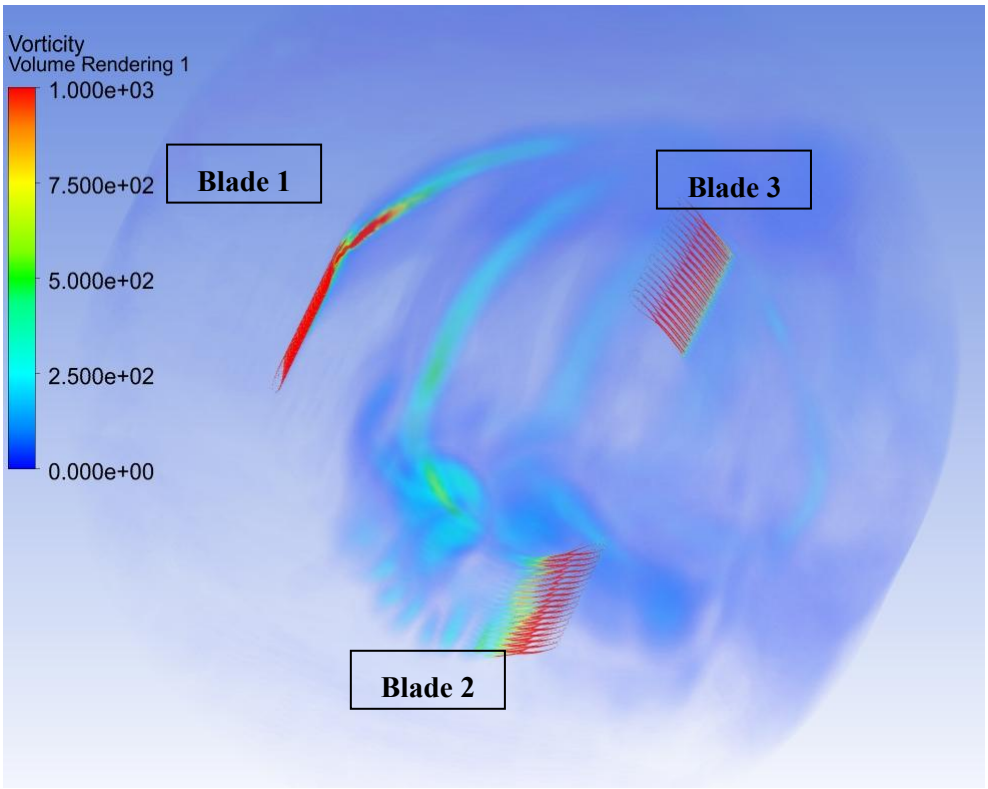

(b) θ = 90°

Cite: T. Syawitri et al., "CFD Investigation of 3D Vertical Axis Wind Turbine Models: Insights from Blade Tip Effects". Evergreen, 12 (04) 2146-2164 (2025). https://doi.org/10.5109/7402644.

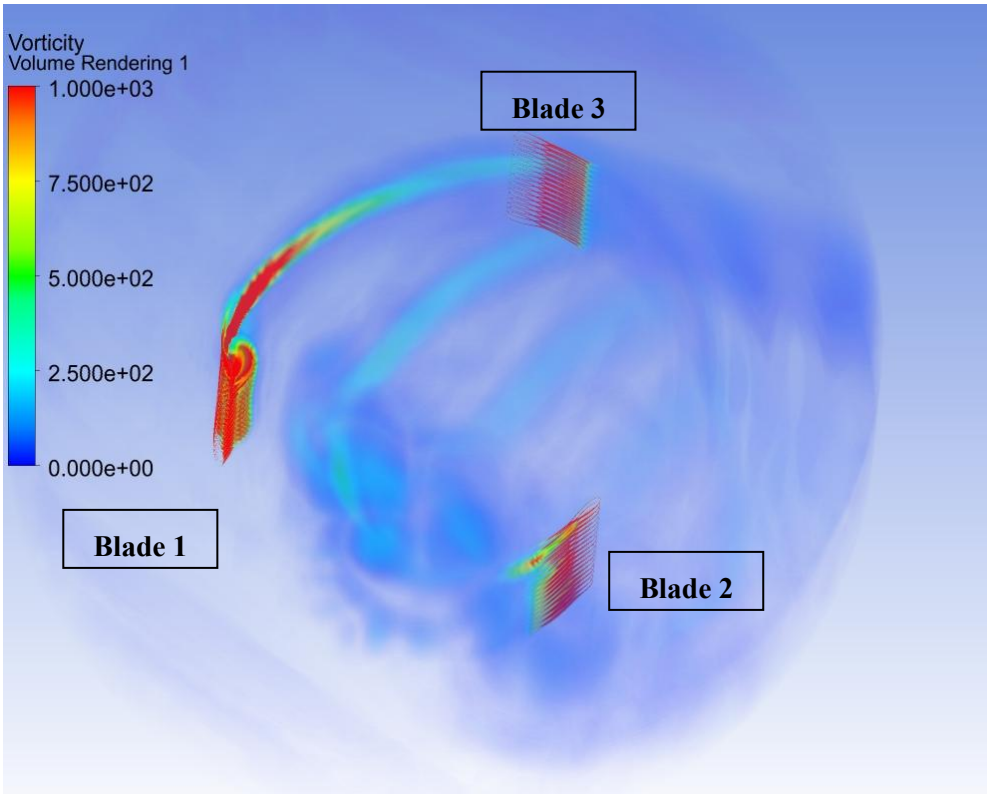

(c) θ = 135°

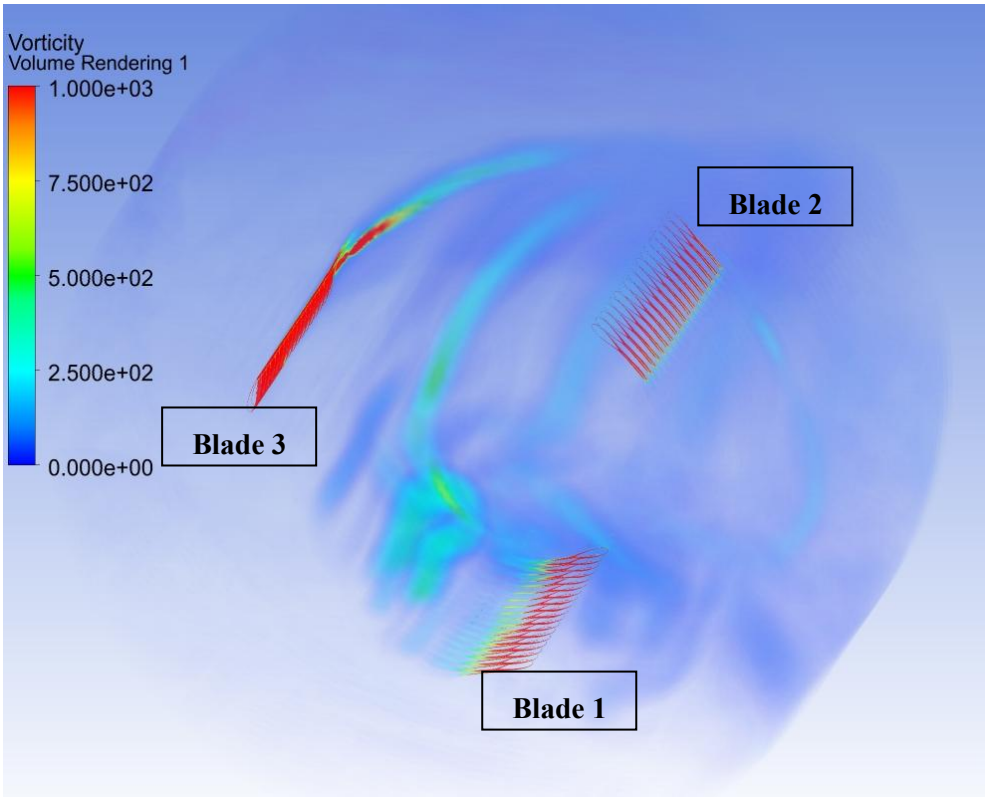

(d) θ = 210°

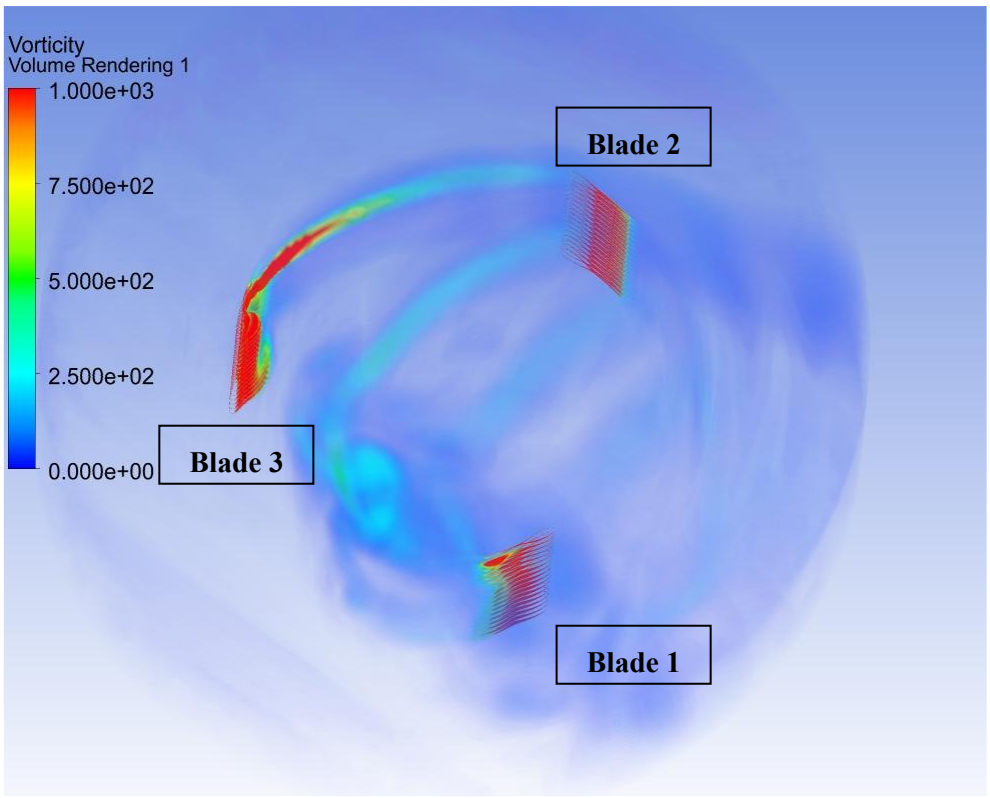

(e) θ = 240°

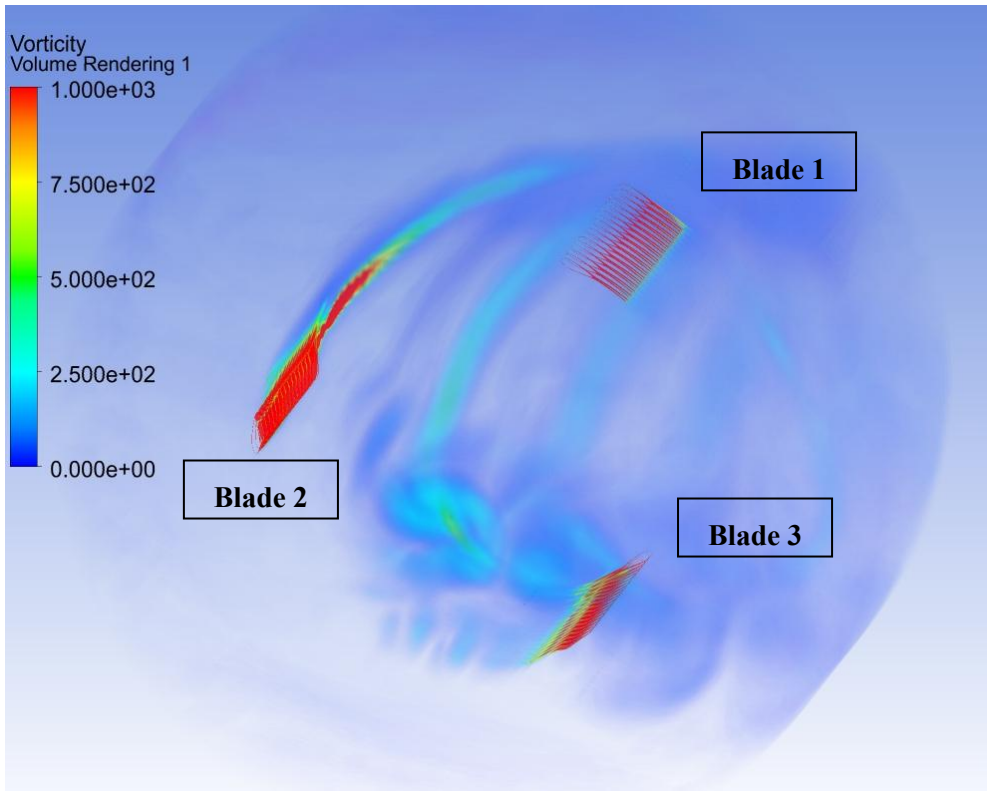

(f) θ = 345°

Fig. 9: Comparison of contour plots of *z*-vorticity at important azimuthal positions

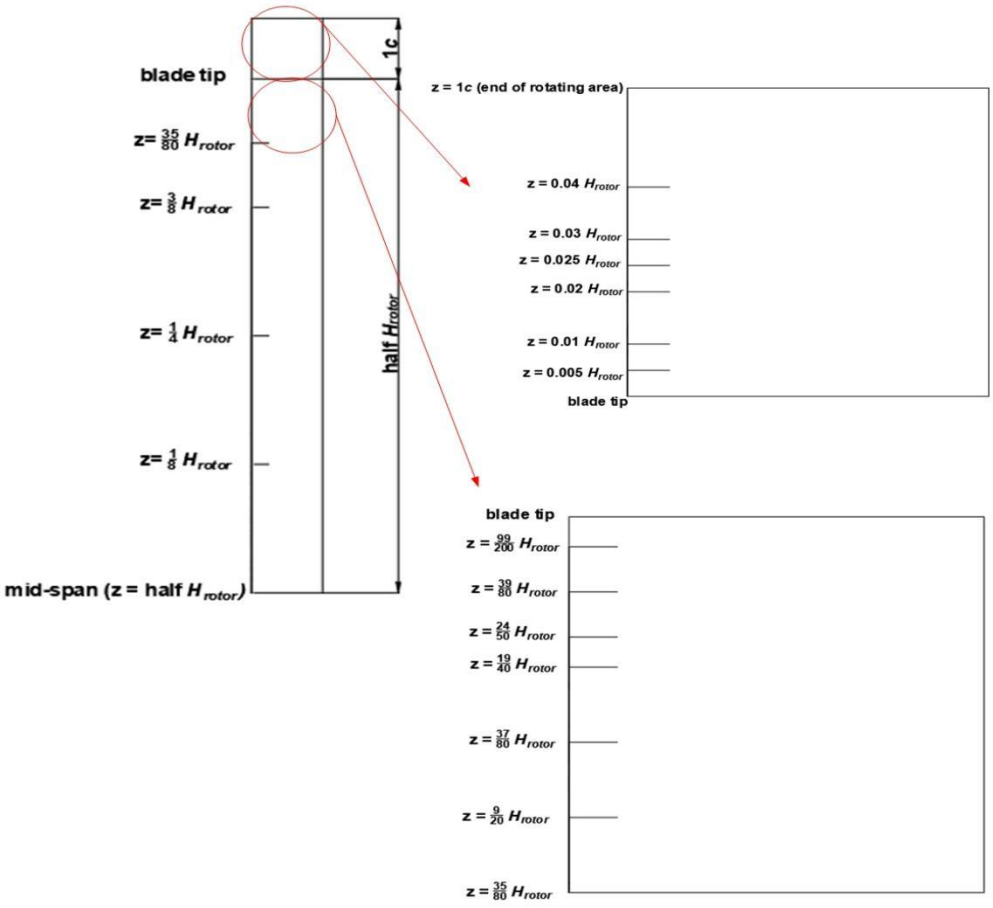
blade tip
1c
z = 1c (end of rotating area)
z= 35/80 H_rotor
z= 3/8 H_rotor
z= 1/4 H_rotor
z= 1/8 H_rotor
half H_rotor
mid-span (z = half H_rotor)
z = 0.04 H_rotor
z = 0.03 H_rotor
z = 0.025 H_rotor
z = 0.02 H_rotor
z = 0.01 H_rotor
z = 0.005 H_rotor
blade tip
blade tip
z = 99/200 H_rotor
z = 39/80 H_rotor
z = 24/50 H_rotor
z = 19/40 H_rotor
z = 37/80 H_rotor
z = 9/20 H_rotor
z = 35/80 H_rotor

(a)

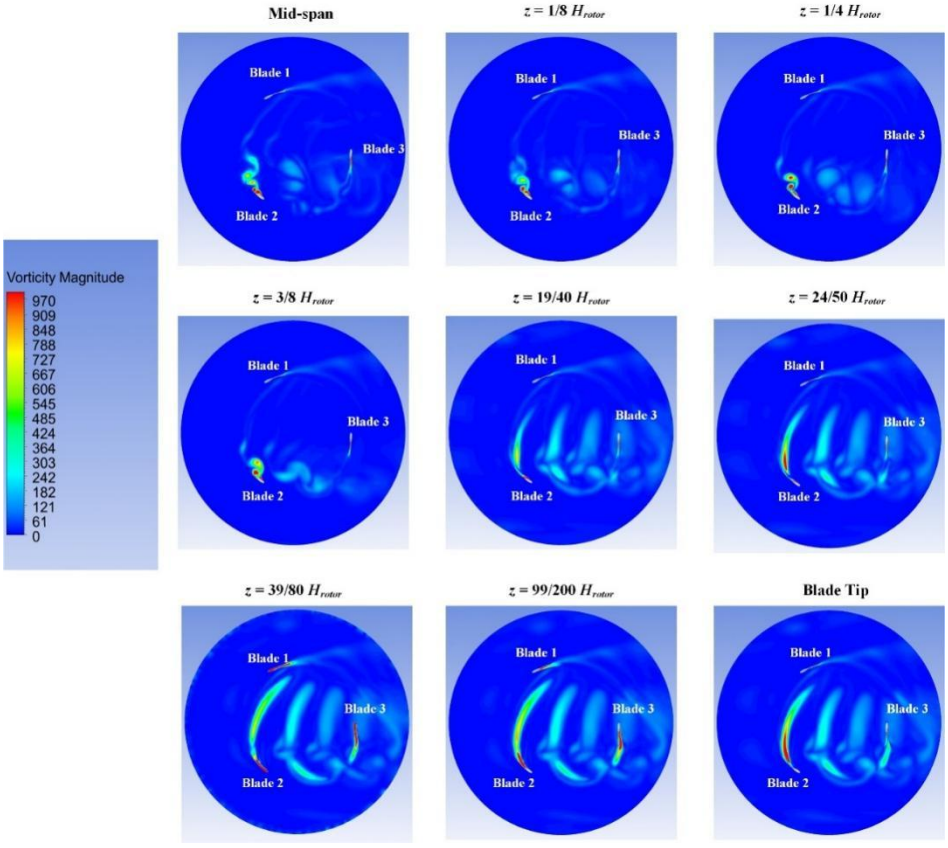
Mid-span
z = 1/8 H_rotor
z = 1/4 H_rotor
z = 3/8 H_rotor
z = 19/40 H_rotor
z = 24/50 H_rotor
z = 39/80 H_rotor
z = 99/200 H_rotor
Blade Tip
Blade 1
Blade 2
Blade 3
Vorticity Magnitude
970
909
848
788
727
667
606
545
485
424
364
303
242
182
121
61
0

(b)

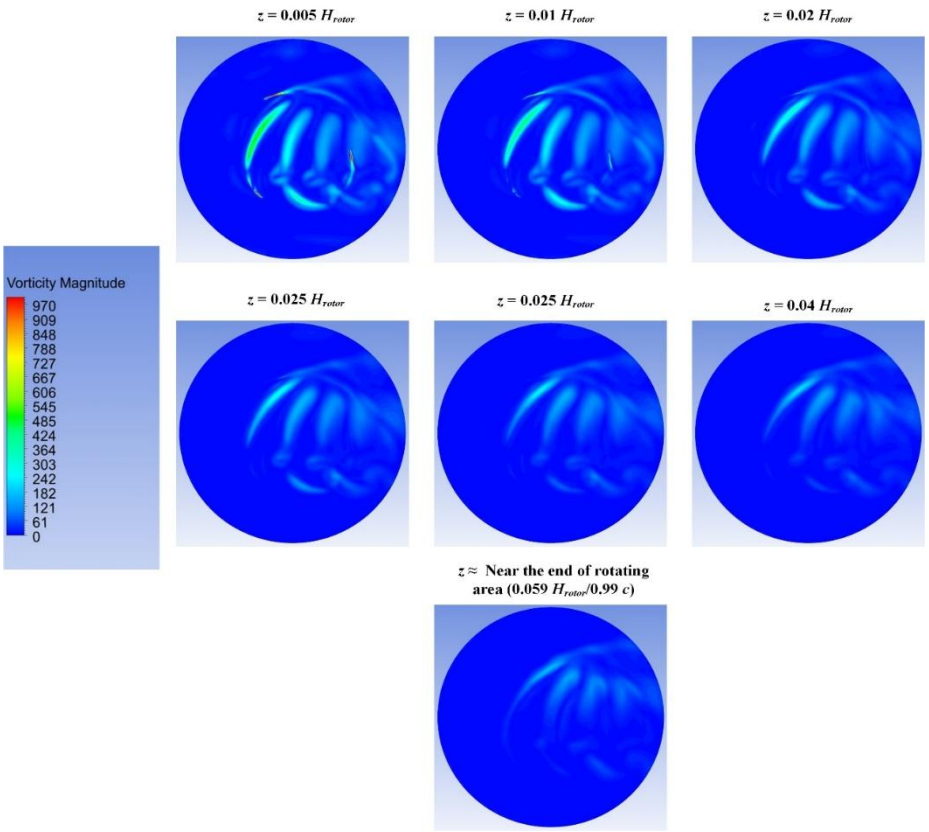

(c)

Fig. 10: Comparison of contour plots of z-vorticity (θ = 30°) at significant span-wise locations: (a) illustration of key span-wise places within the rotating sub-domain, (b) along the blade's midpoint, and (c) from the blade tip to the end point of the rotating zone

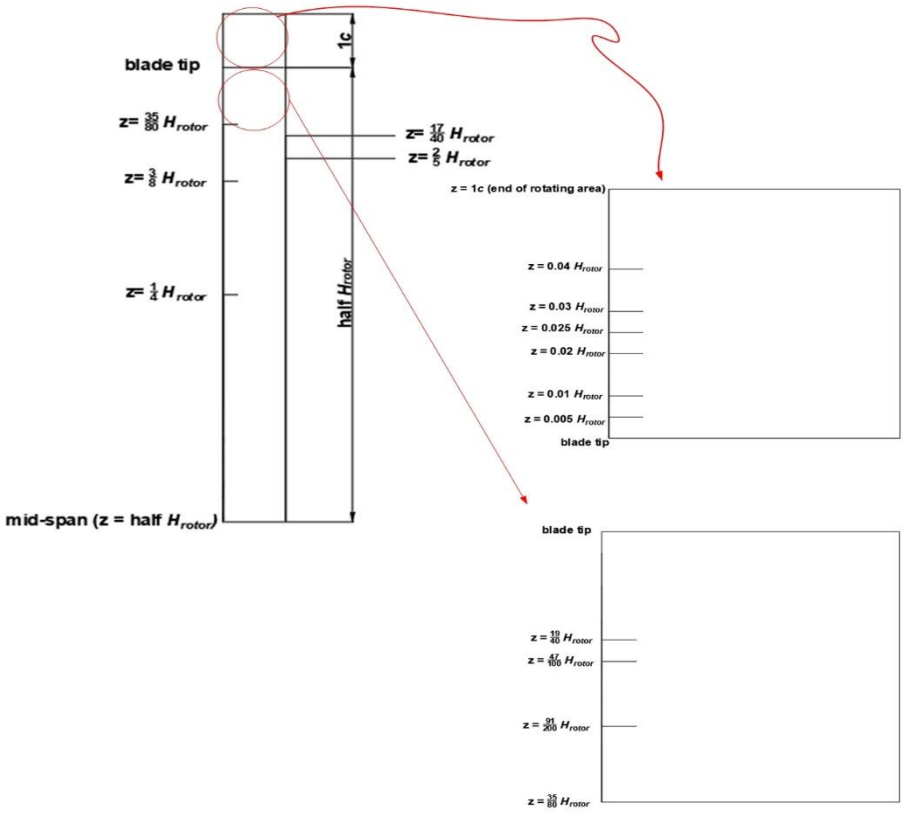

(a)

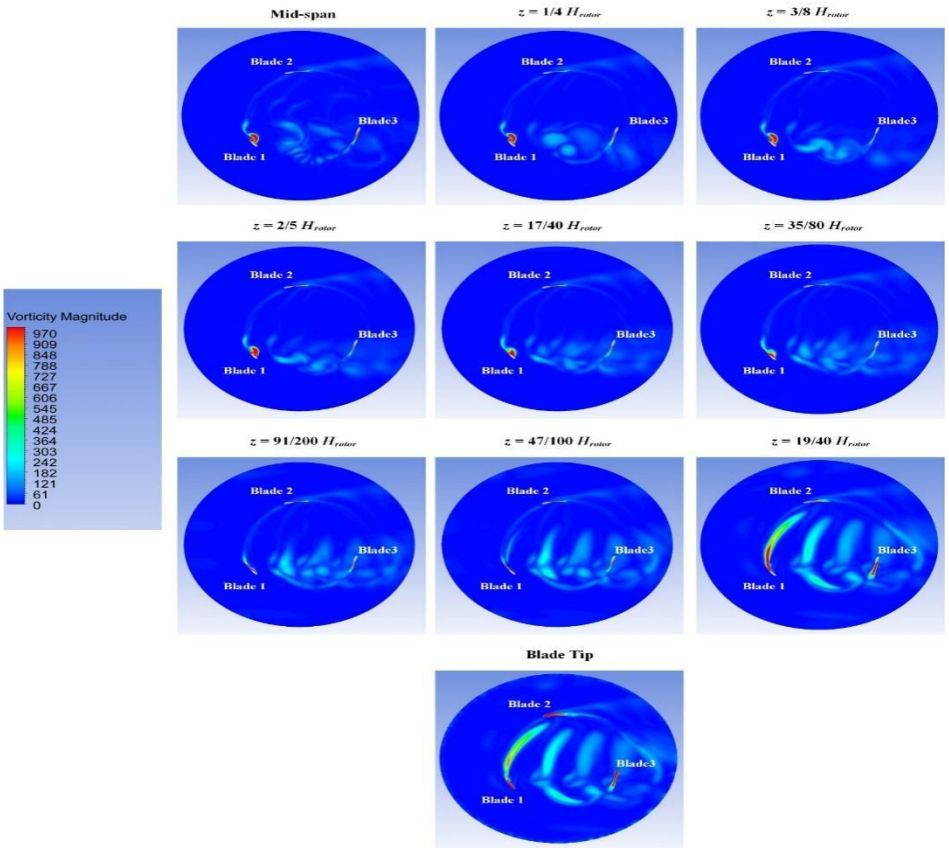

(b)

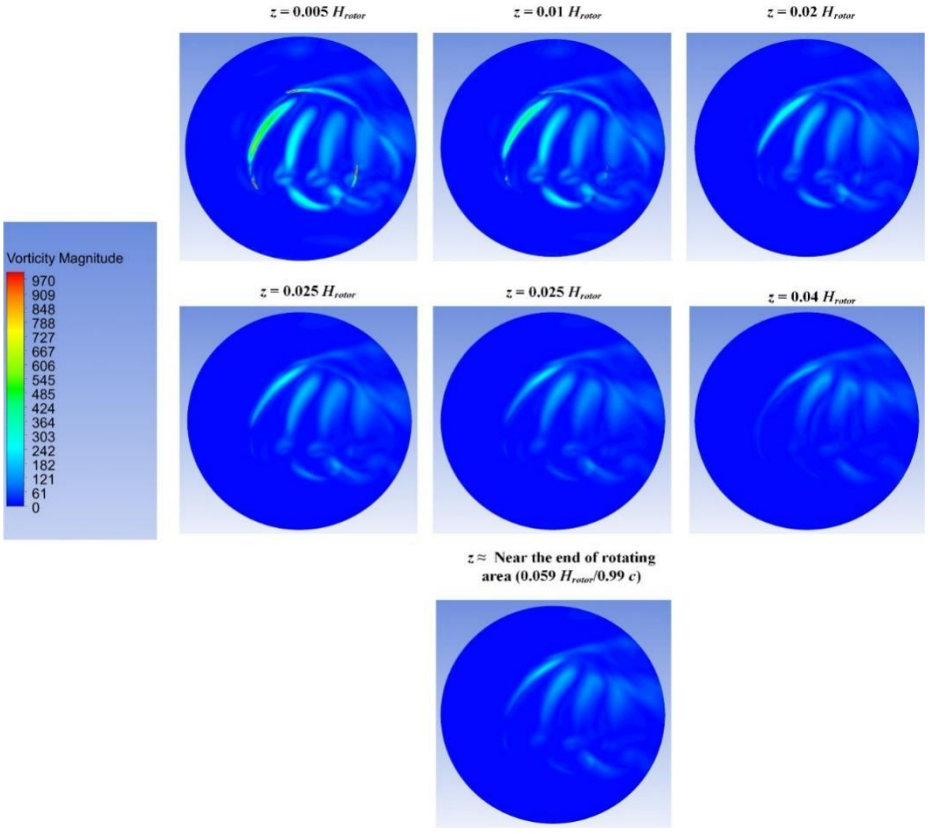

(c)

Fig. 11: Comparison of contour plots of z-vorticity (θ = 135°) at significant span-wise locations: (a) illustration of key span-wise places within the rotating sub-domain, (b) along the blade's midpoint, and (c) from the blade tip to the end point of the rotating zone

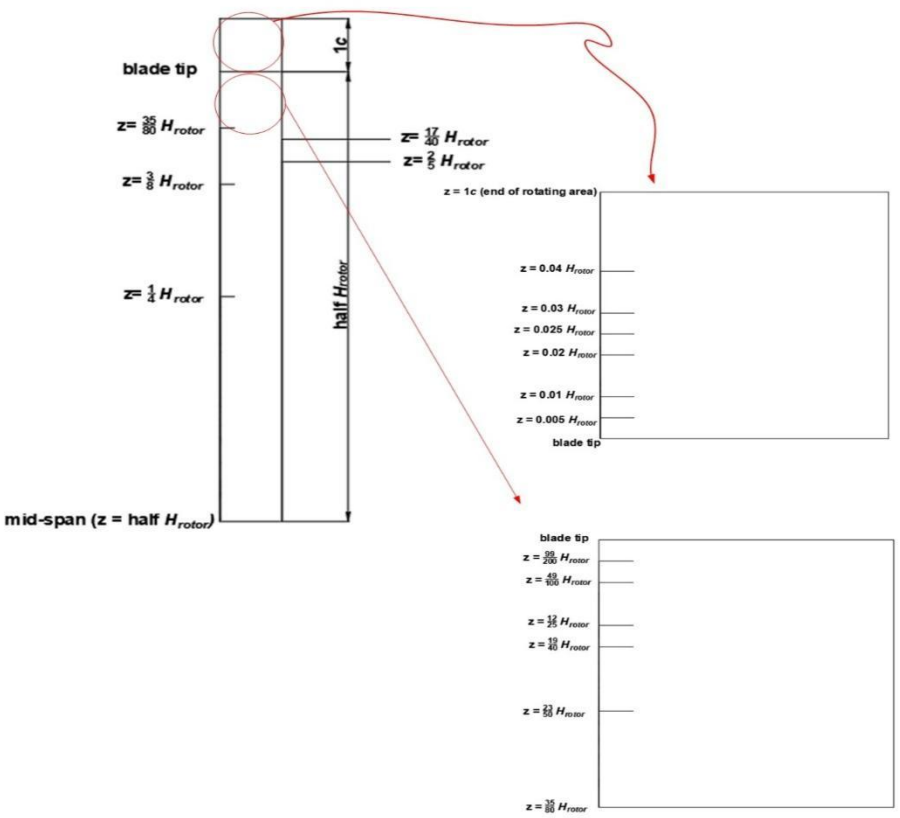
blade tip
1c
z= 35/80 H rotor
z= 17/40 H rotor
z= 2/5 H rotor
z= 3/8 H rotor
z= 1/4 H rotor
half H rotor
mid-span (z = half H rotor)
z = 1c (end of rotating area)
z = 0.04 H rotor
z = 0.03 H rotor
z = 0.025 H rotor
z = 0.02 H rotor
z = 0.01 H rotor
z = 0.005 H rotor
blade tip
blade tip
z = 99/200 H rotor
z = 49/100 H rotor
z = 12/25 H rotor
z = 19/40 H rotor
z = 23/50 H rotor
z = 35/80 H rotor

(a)

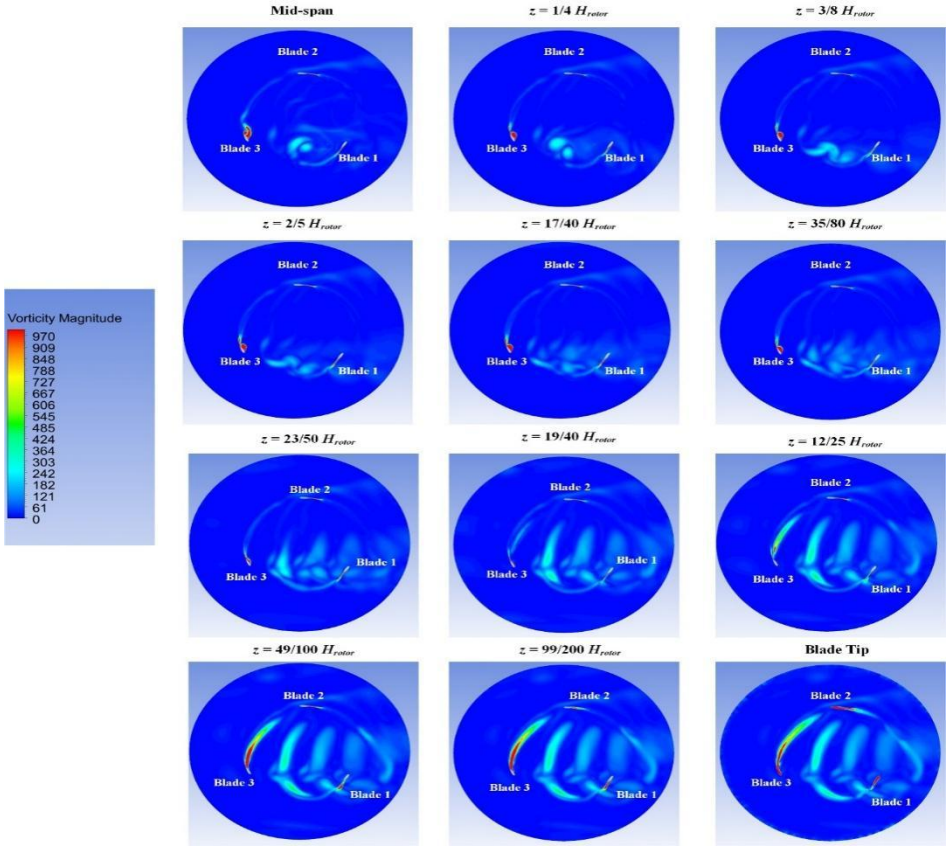
Mid-span
z = 1/4 H rotor
z = 3/8 H rotor
z = 2/5 H rotor
z = 17/40 H rotor
z = 35/80 H rotor
z = 23/50 H rotor
z = 19/40 H rotor
z = 12/25 H rotor
z = 49/100 H rotor
z = 99/200 H rotor
Blade Tip
Blade 1
Blade 2
Blade 3
Vorticity Magnitude
970
909
848
788
727
667
606
545
485
424
364
303
242
182
121
61
0

(b)

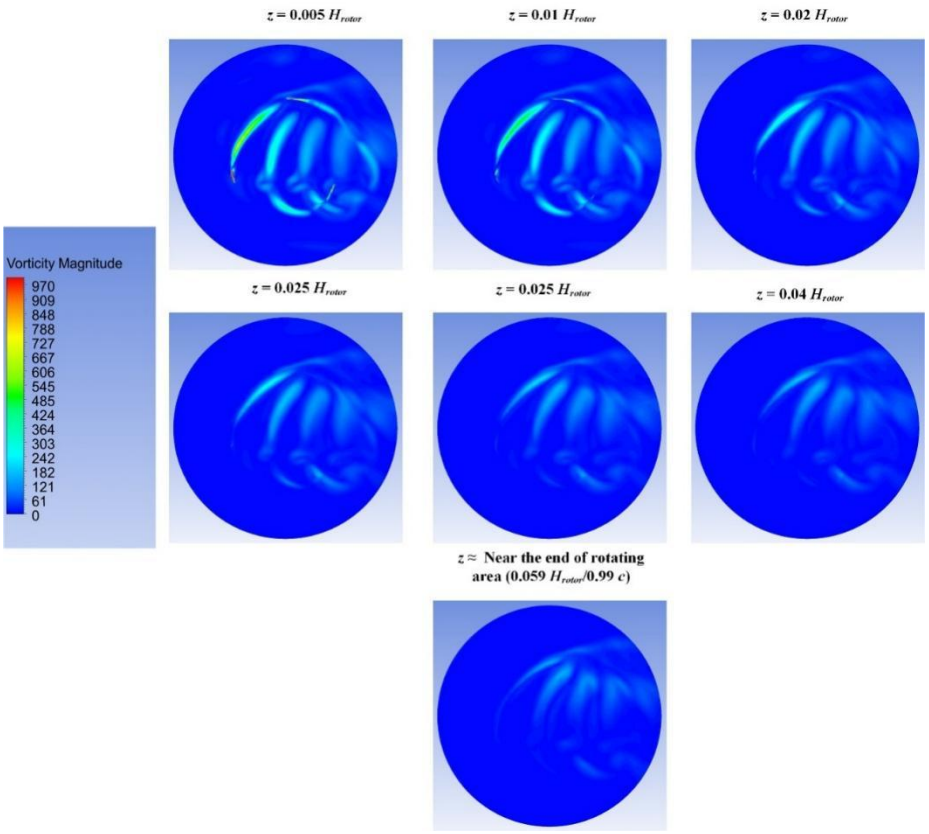

(c)

Fig. 12: Comparison of contour plots of z-vorticity (θ = 240°) at significant span-wise locations: (a) illustration of key span-wise places within the rotating sub-domain, (b) along the blade's midpoint, and (c) from the blade tip to the end point of the rotating zone

Similarly, during θ = 210°–270°, the blade interacts with upstream shed vortices, as illustrated in Figure 9d and Figure. At θ = 240°, a trailing-edge vortex forms and merges with these shed vortices near the blade tip. A secondary vortex appears at z = 12/25 H_{rotor} and coalesces with the primary trailing-edge vortex, culminating in a strong tip vortex near z = 49/100 H_{rotor}. Figure 10c, Figure 11c, and Figure 12c confirm consistent dissipation patterns of blade tip vortices beyond the tip region. Regardless of the azimuthal position, the flow behaviour post-tip remains largely similar, suggesting a predictable aerodynamic pattern outside the blade's physical extent.

6. Conclusion

This study presents a detailed 3D CFD simulation of a VAWT using validated methodologies and advanced discretisation techniques. The model builds upon a previously validated 2D model [41,42], integrating comprehensive boundary conditions and symmetry considerations to enhance computational efficiency. Key insights from the study include:

The study effectively utilises symmetry boundary conditions, reducing computational costs by modelling only half of the rotor blades. This approach aligns with recommendations from previous research [45], ensuring accurate flow simulations while minimising computational effort.

The grid discretisation strategy adopted from the validated 2D model maintains independence in the streamwise x and transverse y directions, while a detailed grid independence study in the span-wise direction confirms that 40 elements along the half of blade height are sufficient for accurate predictions. Additionally, varying the far-field sub-domain discretisation through CutCell meshing optimises computational efficiency while preserving grid quality near critical regions like the blade tip.

The selection of the SBES with Transition SST turbulence model for the 3D simulations is justified by its capability to minimise discrepancies in prediction compared to other turbulence models. However, the study acknowledges the limitations of SBES in accurately capturing dynamic stall and secondary vortex behaviours, leading to a 13.13% average discrepancy in the moment coefficient. Comparatively, the standard SST turbulence model shows improved accuracy with a discrepancy of only 1.17% in 3D simulations, highlighting its potential for enhanced accuracy in future studies.

The analysis of blade aerodynamics reveals significant span-wise variations in the instantaneous moment coefficient, particularly near the blade tip and during

specific azimuthal ranges (45°-150°, 210°-270°). Vorticity contour plots demonstrate distinct vortex behaviours, with pronounced blade tip vortices and trailing-edge vortex interactions contributing to complex flow dynamics. These observations underline the importance of considering span-wise variations in aerodynamic analyses for VAWTs, especially when assessing dynamic stall and vortex interactions.

The 3D model under-predicts the averaged power coefficient compared to experimental data, especially at the blade tip and mid-span regions. Despite this, the discrepancies are consistent with prior studies using similar hybrid RANS-LES models [50,51]. This reinforces the need for continued refinement of turbulence models and experimental validation to improve the accuracy of 3D VAWT simulations.

Overall, the study contributes to the understanding of 3D flow dynamics in VAWTs and highlights the necessity for advanced turbulence modelling and computational approaches to accurately capture complex flow interactions, particularly near the blade tips and during unsteady aerodynamic conditions. Based on the insights gained from the 3D study, future work should focus on refining the turbulence modelling to improve accuracy in simulating three-dimensional flow effects, especially near the blade tip where deviations are more pronounced. Additionally, extending the analysis to include a broader range of rotor configurations and operating conditions would enhance the understanding of aerodynamic performance. Lastly, enhancing computational efficiency through adaptive meshing techniques and incorporating higher-resolution simulations could be pursued to refine the fidelity of results in the far-field and wake regions.

CRediT authorship contribution statement

Taurista Perdana Syawitri: Conceptualisation, Data curation, Formal analysis, Investigation, Methodology, Software, Validation, Visualisation, Writing – original draft

Yufeng Yao: Conceptualisation, Supervision, Writing – review & editing

Jun Yao: Supervision, Writing – review & editing

Budi Chanda: Supervision, Writing – review & editing

Amiral Aziz: Resources, Funding acquisition, Writing – review & editing

Rudi Purwo Wijayanto: Software, Validation, Writing – review & editing

Didik Rostyono: Validation, Writing – review & editing

Arfie Ikhsan Firmansyah: Software, Validation, Writing – review & editing

Agustina Putri Mayasari: Project administration, Writing – review & editing

Ario Witjakso: Project administration, Writing – review & editing

Data availability

Data sets generated during the current study are available from the corresponding author on reasonable request.

Declaration of competing interest

The authors declare no conflicts of interest regarding this manuscript.

Nomenclature

c	chord length (m)
C_m	moment coefficient
C_{m-ave}	averaged moment coefficient
C_{mi}	instantaneous moment coefficient
C_p	power coefficient
C_{p-ave}	averaged power coefficient
E_γ	destruction of intermittency in TSTT turbulence model
f_{SBES}	blending function used in the Stress-Blended Eddy Simulation model
H_{rotor}	rotor's height (m)
i, j, k	index notation corresponding to x, y, z
$P_{\theta t}$	source term for transition onset in TSTT
P_γ	turbulence model
r	production of intermittency in TSTT turbulence
$Re_{\theta t}$	model
	rotor radius (m)
	transition onset momentum-thickness Reynolds number
TSR	tip speed ratio
U	velocity (m/s)
x, y, z	the principal Cartesian directions
y^+	non-dimensional wall distance
Greek symbols	
ρ	fluid density (kg/m^3)
θ	azimuthal position (°)
σ_f	diffusion coefficient for the intermittency
σ_θ	equation
$\tau_{i,j,k}$	diffusion coefficient for the transition-onset momentum-thickness Reynolds number
μ	turbulence stress tensors (N/m^2)
μ_t	dynamic viscosity (Pa.s)
υ_t	turbulence dynamic viscosity (Pa.s)
γ	turbulence kinematic viscosity (m^2/s)
	intermittency

References

1) R. Green, "Experimental methods for aerodynamics," Springer Aerospace Technology, 21–55 (2023). doi:10.1007/978-3-031-12437-2_2.
2) A. E. Romero, A. P. Blasetti, Jansen Gabriel Acosta-López, Miguel-Ángel Gómez-García, and H. de Lasa, "Vorticity and its relationship to vortex separation, dynamic stall, and performance, in an H-Darrieus vertical-axis wind turbine using CFD simulations," Processes, 12 (8) 1556 (2024). doi:10.3390/pr12081556.

3) D. Sharma and R. Goyal, “Methodologies to improve the performance of vertical axis wind turbine: A review on stall formation and mitigation,” Sustainable Energy Technol. Assess., 60, 103561 (2023). doi:10.1016/j.seta.2023.103561.
4) K. Venkatraman, S. Moreau, J. Christophe, and C. Schram, “Numerical investigation of h-Darrieus wind turbine aerodynamics at different tip speed ratios,” International Journal of Numerical Methods for Heat & Fluid Flow, 33 (4) 1489-1512 (2023). doi:10.1108/hff-09-2022-0562.
5) B. Abotaleb, M. M. Takeyeldein, O. Huzayyin, and B. Elhadidi, “Impact of Negative Camber for Performance of Vertical Axis Wind Turbine,” Evergreen 11 (1) 286–294 (2024). doi:10.5109/7172281.
6) A. Ashish and P. Suresh, “Design and analysis of the effect through different aspect ratio on performance of VAWT,” Lecture notes in mechanical engineering 333–340 (2022). doi:10.1007/978-981-19-1618-2_32.
7) N. Franchina, O. Kouaissah, G. Persico, and M. Savini, “Three-dimensional CFD simulation and experimental assessment of the performance of a H-Shape vertical-axis wind turbine at design and off-design conditions,” International Journal of Turbomachinery, Propulsion and Power 4 3 30 (2019). doi:10.3390/ijtpp4030030.
8) D. M. Prabowoputra, A. R. Prabowo, I. Yaningsih, D. D. D. P. Tjahjana, F. B. Laksono, R. Adiputra, and H. Suryanto, “Effect of Blade Angle and Number on the Performance of Bánki Hydro-Turbines: Assessment using CFD and FDA Approaches,” Evergreen 10 (1) 519–530 (2023). doi:10.5109/6782156.
9) I. Yaningsih, D. D. D. P. Tjahjana, E. P. Budiana, M. Muqoffa, Z. Arifin, S. Suyitno, K. Enoki, dan T. Miyazaki, "Numerical study on the Effect of Rectangular and Triangular Counter-Rotating Vortex Generators on the H-Rotor Wind Turbine Performance," Evergreen 10 (1) 230–241 (2023). doi:10.5109/6781073.
10) O. M. A. M. Ibrahim and S. Yoshida, “Experimental and Numerical Studies of a Horizontal Axis Wind Turbine Performance over a Steep 2D Hill,” Evergreen 5 (3) 12–21 (2018). doi:10.5109/1957496.
11) A. Hijazi, A. ElCheikh, and M. Elkhoury, “Numerical investigation of the use of flexible blades for vertical axis wind turbines,” Energy Convers. Manage., 299 117867 (2024). doi:10.1016/j.enconman.2023.117867.
12) S. ed-Dîn Fertahi, T. Belhadad, A. Kanna, A. Samaouali, I. Kadiri, and E. Benini, “A Critical Review of CFD Modeling Approaches for Darrieus Turbines: Assessing Discrepancies in Power Coefficient Estimation and Wake Vortex Development,” Fluids 8 (9) 242 (2023). doi:10.3390/fluids8090242.
13) B. Anggara, E. P. Budiana, C. Harsito, K. Enoki, K.-S. Kim, I. Yaningsih, D. D. D. P. Tjahjana, "Performance Improvement of H-Darrieus Wind Turbine with High Efficiency Vortex Structure Attachment," Evergreen 10 (1) 496-503 (2023). doi: 10.5109/6782153.
14) O. Eboibi, B. E. Eboibi, and L. A. M. Danao, “Solidity effects and azimuth angles on flow field aerodynamics and performance of vertical axis wind turbines at low Reynolds number,” Scientific African, 24 e02215 (2024). doi:10.1016/j.sciaf.2024.e02215.
15) T. P. Syawitri, Y. Yao, J. Yao, and B. Chandra, “Geometry optimisation of vertical axis wind turbine with Gurney flap for performance enhancement at low, medium and high ranges of tip speed ratios,” Sustainable Energy Technol. Assess.,, 49 101779 (2022). doi:10.1016/j.seta.2021.101779.
16) N. Franchina, G. Persico, and M. Savini, “2D-3D Computations of a Vertical Axis Wind Turbine Flow Field: Modeling Issues and Physical Interpretations,” Renewable Energy, 136 1170–1189 (2019). doi: 10.1016/j.renene.2018.09.086.
17) S. Sanaye and A. Farvizi, “Optimizing a vertical axis wind turbine with helical blades: Application of 3D CFD and Taguchi method,” Energy Reports 12 2547 (2024). doi:10.1016/j.egyr.2024.08.059.
18) N. Franchina, O. Kouaissah, G. Persico, and M. Savini, “Three-dimensional modeling and investigation of the flow around a troposkein vertical axis wind turbine at different operating conditions,” Renewable Energy, 199 368–38 (2022). doi:10.1016/j.renene.2022.08.130.
19) B. Hand, G. Kelly, and A. Cashman, “Numerical simulation of a vertical axis wind turbine airfoil experiencing dynamic stall at high Reynolds numbers,” Computers & Fluids, 149 12–30 (2017). doi:10.1016/j.compfluid.2017.02.021.
20) A.-J. Buchner, M. W. Lohry, L. Martinelli, J. Soria, and A. Smits, “Dynamic stall in vertical axis wind turbines: Comparing experiments and computations,” J. Wind Eng. Ind. Aerodyn., 146 163–171 (2015). doi:10.1016/j.jweia.2015.09.001.
21) A. Aulia, A. S. Rofi’i, M. F. Fadri, M. H. Syarif, G. D. Haryadi, E. Susanto, "Numerical Investigation on the Torque Yields of the Darrieus Turbine with Various Deflectors Shape and Distance," Evergreen, 11 (4) 3290-3298 (2024). doi:10.5109/7326963.
22) D. D. D. P. Tjahjana, M. J. H. As-Sidqi, E. P. Budiana, K. Enoki, and I. Yaningsih, “Rectangular Straight Vortex Generator Performance Analysis for H Rotor Darrieus Turbine,” Evergreen, 11 (3) 2332–2341 (2024). doi:10.5109/7236876.
23) H. Y. Peng, X. R. Yang, H. J. Liu, and S. Y. Sun,

"Aerodynamic analysis of vertical axis wind turbines at various turbulent levels: Insights from 3D LES simulations," Journal of Building Engineering, 94 109899 (2024). doi:10.1016/j.jobe.2024.109899.

24) R. Farzadi, A. Zanj, and M. Bazargan, "Effect of baffles on efficiency of darrieus vertical axis wind turbines equipped with J-type blades," Energy, 305 132305 (2024). doi:10.1016/j.energy.2024.132305.
25) G. M. Avalos, N. R. Hau, R. Quintal-Palomo, E.E. Ordóñez López, M. Gamboa-Marrufo, and M. A. E. Soberanis, "Aerodynamic techniques to mitigate the 3D loss in the power coefficient of vertical axis wind turbines," Energy Convers. Manage., 311 118507 (2024). doi:10.1016/j.enconman.2024.118507.
26) A. Sheidani, S. Salavatidezfouli, G. Stabile, and G. Rozza, "Assessment of URANS and LES methods in predicting wake shed behind a vertical axis wind turbine," J. Wind Eng. Ind. Aerodyn., 232 105285 (2023). doi:10.1016/j.jweia.2022.105285.
27) J. T. Hansen, M. Mahak, and I. Tzanakis, "Numerical modelling and optimization of vertical axis wind turbine pairs: A scale up approach," Renewable Energy, 171 1371–1381 (2021). doi:10.1016/j.renene.2021.03.001.
28) P. Zheng, H. Zhang, Z. Zhang, W. Salman, and M. Abdelrahman, "Parameter optimization method of contra-rotating vertical axis wind turbine: Based on numerical simulation and response surface," J. Cleaner Prod., 435 140475 (2023). doi:10.1016/j.jclepro.2023.140475.
29) R. Zhao, Angus, Y. Li, V. Venugopal, and L. Borthwick, "Numerical analysis of the performance of a three-bladed vertical-axis turbine with active pitch control using a coupled unsteady Reynolds-averaged Navier-Stokes and actuator line model," Journal of hydrodynamics/Journal of Hydrodynamics. Ser. B, 35 (3) 516–532 (2023). doi:10.1007/s42241-023-0035-x.
30) B. Abotaleb, M. M. Takeyeldein, O. Huzayyin, and B. Elhadidi, "Impact of Negative Camber for Performance of Vertical Axis Wind Turbine," Evergreen, 11 (1) 286–294 (2024). doi:10.5109/7172281.
31) A. Aihara, K. Bolin, A. Goude, and H. Bernhoff, "Aeroacoustic noise prediction of a vertical axis wind turbine using large eddy simulation," International Journal of Aeroacoustics, 20 8 959–978 (2021). doi:10.1177/1475472x211055179.
32) A. Posa, "Dependence of the wake recovery downstream of a Vertical Axis Wind Turbine on its dynamic solidity," J. Wind Eng. Ind. Aerodyn.,, 202 104212 (2020). doi:10.1016/j.jweia.2020.104212.
33) J. Su, H. Lei, D. Zhou, Z. Han, Y. Bao, H. Zhu, and L. Zhou, "Aerodynamic noise assessment for a vertical axis wind turbine using Improved Delayed Detached Eddy Simulation," Renewable Energy 141 559–569 (2019). doi:10.1016/j.renene.2019.04.038.
34) W. Xu, G. Li, X. Zheng, Y. Li, S. Li, C. Zhang, and F. Wang, "High-resolution numerical simulation of the performance of vertical axis wind turbines in urban area: Part I, wind turbines on the side of single building," Renewable Energy, 177 461–474 (2021). doi:10.1016/j.renene.2021.04.071.
35) W. Xu, Y. Li, G. Li, S. Li, C. Zhang, and F. Wang, "High-resolution numerical simulation of the performance of vertical axis wind turbines in urban area: Part II, array of vertical axis wind turbines between buildings," Renewable Energy, 176 25-39 (2021). doi:10.1016/j.renene.2021.05.011.
36) W. Miao, Q. Liu, Z. Xu, M. Yue, C. Li, and W. Zhang, "A comprehensive analysis of blade tip for vertical axis wind turbine: Aerodynamics and the tip loss effect," Energy Convers. Manage., 253 115140 (2022). doi:10.1016/j.enconman.2021.115140.
37) B. Hand, "Three-dimensional computational fluid dynamic analysis of a large-scale vertical axis wind turbine," Wind Engineering, 42 2, 0309524X2110379 (2021). doi:10.1177/0309524x211037911.
38) Q. Tang, Y. Wu, A. Yu, B. Peng, Y. Wang, and J. Lyu, "Investigation of energy dissipation of an H-type vertical axis wind turbine based on entropy production theory," Energy Conversion and Management, 283 116953 (2023). doi:10.1016/j.enconman.2023.116953.
39) T. Zhang, M. Elsakka, W. Huang, Z. Wang, D. B. Ingham, L. Ma, and M. Pourkashanian, "Winglet design for vertical axis wind turbines based on a design of experiment and CFD approach," Energy Convers. Manage., 195 712–726 (2019). doi:10.1016/j.enconman.2019.05.055.
40) J. Radhakrishnan, S. Sridhar, M. Zuber, E. Y. K. Ng, and S. S. B., "Design optimization of a Contra-Rotating VAWT: A comprehensive study using Taguchi method and CFD," Energy Convers. Manage., 298 117766 (2023). doi:10.1016/j.enconman.2023.117766.
41) T. P. Syawitri, Y. F. Yao, B. Chandra, and J. Yao, "Comparison study of URANS and hybrid RANS-LES models on predicting vertical axis wind turbine performance at low, medium and high tip speed ratio ranges," Renewable Energy, 168 247–269 (2021). doi:10.1016/j.renene.2020.12.045.
42) T. P. Syawitri, Y. Yao, J. Yao, and B. Chandra, "Assessment of stress-blended eddy simulation model for accurate performance prediction of vertical axis wind turbine," International Journal of Numerical Methods for Heat & Fluid Flow, 31 2 655–673 (2020). doi:10.1108/hff-09-2019-0689.
43) R. Howell, N. Qin, J. Edwards, and N. Durrani,

"Wind tunnel and numerical study of a small vertical axis wind turbine," Renewable Energy, 35 (2) 412–422 (2010). doi:10.1016/j.renene.2009.07.025.

44) M. R. Castelli, A. Englaro, and E. Benini, "The Darrieus wind turbine: Proposal for a new performance prediction model based on CFD," Energy, 36 8 4919–4934 (2011). doi:10.1016/j.energy.2011.05.036.
45) M. Elsakka, "The aerodynamics of fixed and variable pitch vertical axis wind turbine," Ph.D thesis. University of Sheffield, Sheffield, United Kingdom, 2020.
46) C. Hofemann, C. S. Ferreira, K. Dixon, G. van Bussel, G. van Kuik, and F. Scarano, "3D stereo PIV study of tip vortex evolution on a VAWT," Proceedings of 2008 European Wind Energy Conference and Exhibition European Wind Energy Association, 1-8 (2008).
47) ANSYS Inc., "ANSYS Meshing User's Guide," Canonsburg, 2010.
48) M. R. Castelli, G. Ardizzon, L. Battisti, E. Benini, and G. Pavesi, "Modeling strategy and numericalvalidation for a Darrieus vertical axis micro-wind turbine," ASME Proceedings of ASME 2010 International Mechanical Engineering Congress & Exposition, 409-418 (2010).
49) Y. Wang, S. Shen, G. Li, D. Huang, and Zhongquan Charlie Zheng, "Investigation on aerodynamic performance of vertical axis wind turbine with different series airfoil shapes," Renewable Energy, 126 801–818 (2018). doi:10.1016/j.renene.2018.02.095.
50) M. F. Alam, D. Thompson, and D. K. Walters, "Critical assessment of hybrid RANS-LES modeling for attached and separated flows," in Turbulence Modelling Approaches - Current State, Development Prospects, Applications. IntechOpen, 2017. https://www.intechopen.com/chapters/56282 [Accessed 02 November 2021].
51) H. Lei, D. Zhou, Y. Bao, Y. Li, and Z. Han, "Three-dimensional Improved Delayed Detached Eddy Simulation of a two-bladed vertical axis wind turbine," Energy Convers. Manage., 133 235–248 (2017). doi:10.1016/j.enconman.2016.11.067.
52) A. Rezaeiha, H. Montazeri, and B. Blocken, "On the accuracy of turbulence models for CFD simulations of vertical axis wind turbines," Energy, 180 838–857 (2019). doi:10.1016/j.energy.2019.05.053.